

www.acsami.org Research Article

Direct-Write Printing Copper-Nickel (Cu/Ni) Alloy with Controlled Composition from a Single Electrolyte Using Co-Electrodeposition

Chao Wang, Md Emran Hossain Bhuiyan, Salvador Moreno, and Majid Minary-Jolandan*



Cite This: https://dx.doi.org/10.1021/acsami.0c01100



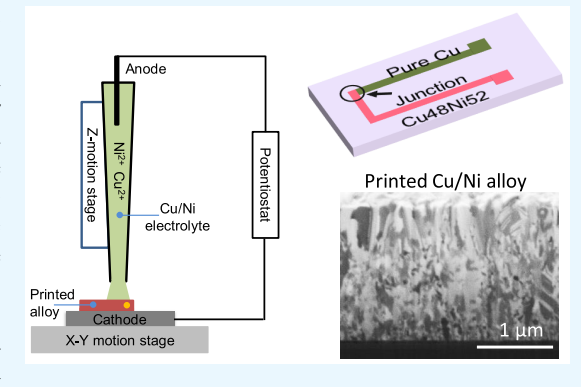
ACCESS

III Metrics & More

Article Recommendations

Supporting Information

ABSTRACT: Although various processes for metal printing at the microand mesoscale have been demonstrated, printing functional devices such as thermocouples, thermopiles, and heat flux sensors that function based on interfaces between an alloy and another alloy/metal demands processes for printing alloys. Furthermore, a high-quality and crystalline alloy is required for acceptable function of these devices. This article reports for the first time co-electrodeposition-based printing of single-phase solid solution nanocrystalline copper/nickel (Cu/Ni) alloy with various controllable compositions (Cu100Ni0 to Cu19Ni81) from a single electrolyte. The printed alloy is nanocrystalline (<35 nm), continuous, and dense with no apparent porosity, with remarkable mechanical and magnetic properties, without any postprocessing annealing such as heat treatment. In addition, a functional thermocouple fabricated using this process is demonstrated. Such



a process can not only be used for fabrication of functional devices, it may also facilitate fundamental studies on alloys by printing a continuous library of alloy composition for material characterization.

KEYWORDS: direct-write printing, confined electrodeposition, alloy printing, copper/nickel alloy, co-electrodeposition, mechanical properties, magnetic properties

■ INTRODUCTION

Micro- and mesoscale additive printing, often in combination with traditional microfabrication processes, have emerged as low-cost and versatile processes for fabrication of sensors and electronic devices. These processes include direct ink writing (DIW),²⁻⁴ electrohydrodynamic printing (EHD),^{5,6} laser-induced forward transfer (LIFT),⁷⁻⁹ focused electron/ion beam induced deposition (FEBID/FIBID), ¹⁰ laser-induced photoreduction (LIPR), ^{11,12} and meniscus confined electrodeposition, ^{13–15} among others. Although metals are of interest for conductive traces in devices and sensors, functional devices such as thermocouples and heat flux sensors often require an interface between an alloy and a metal/alloy. Furthermore, a high quality and crystalline alloy is required for acceptable function of the device. Laser transfer of alloys from bulk phase molten metal for digital microfabrication of three-dimensional (3D) objects has been reported. 16 Direct writing using liquid metal has been reported for fabrication of thermocouples and electronics, including flexible electronics. 17-19 Direct-write thermal spray (DWTS) is one of the processes that has been explored for additive fabrication of sensor circuits on complexshaped components.²⁰ DWTS is a process that sprays accelerated materials on a substrate and creates dense and strongly adherent deposits. A similar process is used to apply a thermal barrier coating (TBC) on various components. Thermocouples using DWTS have been reported. 20-22 In

addition, capacitive strain gauges have been also fabricated using combined DWTS process and laser micromachining. Screen printing has been also reported to print thermocouple and other electronics. So far, microscale additive printing processes that allow for direct printing of high-quality crystalline alloys have not been reported. This article reports the novel co-electrodeposition-based printing of nanocrystalline copper/nickel (Cu/Ni) alloy with controllable composition (Cu100Ni0 to Cu19Ni81) from a single electrolyte for the first time.

Electrodeposition is one of the most common processes for fabrication of metals and alloys for various devices such as in microelectronics, sensors, and energy conversion devices. Co-electrodeposition of various binary and ternary alloys such as nickel—cobalt, ^{27,28} cobalt tungsten, ²⁸ nickel—copper, ²⁹ nickel—tungsten, ^{30–33} nickel—molybdenum, ³¹ cobalt molybdenum and cobalt tungsten, ³⁴ and lead—tin, ³⁵ among others have been reported using conventional electroplating processes from various electrolytes such as aqueous, molten salt, and ionic

Received: January 18, 2020 Accepted: March 30, 2020 Published: March 30, 2020



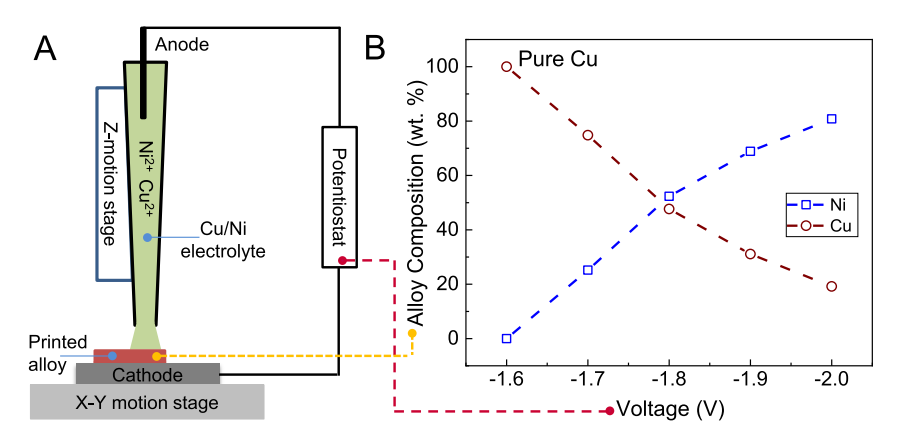


Figure 1. (A) The schematic illustration of the Cu/Ni alloy printing process. (B) The dependence of the alloy composition deposited from the single electrolyte on the applied potential.

liquid. Alloy microstructure (crystalline vs amorphous) can vary based on the electrolyte composition, applied potential (current density), and presence of additives in the electrolyte. In particular, nanocrystalline and nanotwinned microstructures can be obtained, for example, by application of pulsed current voltage. 30,32,33,36 Electrodeposition of alloys is often with the aim of obtaining functionalities such as enhanced thermal stability, magnetic properties, magnetoresistance, coating applications, etc. 30,37-39 Additionally, nanocomposite coatings can be electrodeposited by mixing nanoparticles with the alloy electrolyte, such as NiW/SiC nanocomposite. 40 Another attractive application of electrodeposition of alloys is in fabrication of functional devices, such as strain sensors, thermocouples, and heat flux sensors. In particular, the combination of direct-write electrochemical printing and traditional microfabrication processes results in powerful processes for direct printing of metals and alloys, 41-43 which reduces several steps involved in traditional microfabrication for thin film sensors. 44,45

In this article, probe-based printing of Cu/Ni alloy is reported. The printed alloy is nanocrystalline (<35 nm), continuous, and dense with no apparent porosity, with remarkable mechanical and magnetic properties, without any postprocessing annealing such as heat treatment. In addition, a functional thermocouple fabricated using this process is demonstrated. To our knowledge, this is the first demonstration of direct printing of nanocrystalline alloys toward functional device fabrication. Such process not only can be used for fabrication of functional devices; in addition, it may facilitate fundamental studies on alloys by printing a continuous library of alloy composition for material characterization. ⁴⁶

■ RESULTS AND DISCUSSION

The schematic view of the alloy printing process is shown in Figure 1A. Fundamentally, the process is based on the conventional electroplating (electrodeposition) process. A nozzle with a few microns to millimeters tip diameter, containing the alloy electrolyte, functions as the printing head. ^{13,14} In this process, printing starts when a potential/current is applied to the circuit between the anode in the nozzle and the cathode, which in this case is the substrate. The precise motion of positioning stages along the *X*- and *Y*-directions, and the nozzle along the *Z*-direction results in printing of desired Cu/Ni alloy patterns.

The electrolyte bath used in this study was formulated by Green⁴⁷ and contains 0.04 M CuSO₄·5H₂O and 0.7 M NiSO₄·6H₂O. Cyclic voltammograms of the electrolyte is shown in Figure S1. On the basis of the Nernst equation:²⁶

$$E_{\rm eq}(M) = E_{\rm M^{n+}}^0 + (RT/nF) \ln a_{\rm M^{n+}}$$
 (1)

where $E_{\rm eq}({\rm M})$ is the redox potential of the reaction ${\rm M}^{n+}$ + $ne \rightarrow {\rm M}$, $E_{{\rm M}^{n+}}^0$ is the standard redox potential for metal M ($E_{{\rm N}i^{2+}}^0$ is -0.25 V, $E_{{\rm Cu}^{2+}}^0$ is +0.34 V), R is the gas constant, T is the absolute temperature, n is the number of electrons exchanged, F is the Faraday constant, and $a_{{\rm M}^{n+}}$ is the activity of the ion ${\rm M}^{n+}$. For codeposition to occur, the redox potentials of species must be as close as possible to each other. In eq. 1, the redox potential can be changed by changing the ions' activity. Sodium citrate is added to the electrolyte as the complexant, and its complexation with metal ions significantly changes the metal ions activity. The complexing agent was required as the standard reduction potentials for Cu (+0.34 V) and Ni (-0.25 V) are quite different, and hence the codeposition of these metals requires that a complexing agent is added to the electrolyte.

During the codeposition, complexant ion discharge reactions occur at the cathode: 49

$$NiCit^{-} \rightarrow Ni^{2+} + Cit^{3-}$$
 (2)

$$Ni^{2+} + 2e \rightarrow Ni \tag{3}$$

$$CuCit^{-} \rightarrow Cu^{2+} + Cit^{3-}$$
 (4)

$$Cu^{2+} + e \rightarrow Cu^{+} \tag{5}$$

$$Cu^+ + e \rightarrow Cu$$
 (6

It is known that in citrate-containing electrolytic solutions, Ni deposition is charge-transfer controlled, whereas that of Cu is mass-transfer-controlled. Deposition is enhanced, while electroactive Cu species at the electrolyte/working-electrode interface get depleted, thus providing nickel-rich deposits. Figure 1B shows the dependence of the alloy composition deposited from the single electrolyte on the applied potential. The composition was obtained from energy-dispersive X-ray spectroscopy (EDS) analysis. The EDS spectra are presented in Figure S5. By decreasing the applied voltage from -1.6 V to -2.0 V, the alloy composition is varied from Cu100Ni0 to Cu19Ni81. This trend is similar to that reported for bulk electroplating of Cu/Ni alloy thin films. S2,53 On the basis of

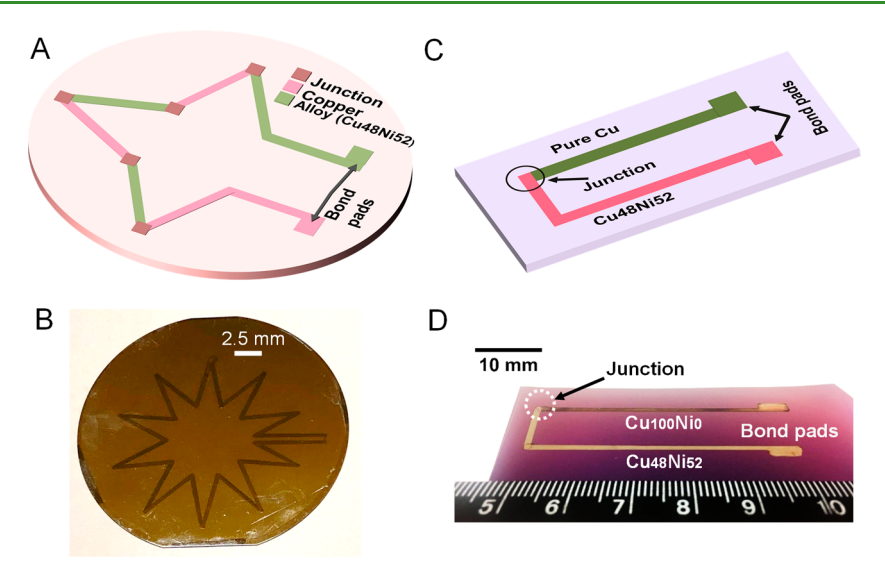


Figure 2. Demonstration of potential applications of the process: (A) and (B) a thermopile, and (C) and (D) a thin film thermocouple. The legs are pure Cu and Cu48Ni52 alloy, both deposited from the same electrolyte by applying -1.6 V for Cu and -1.8 V for Cu48Ni52 alloy.

our data and the literature, pure Cu (Cu100Ni0) can be obtained from this alloy; 54 however, at voltage <-2 V, hydrogen evolution and the resulting bubble formation prevent pure Ni from depositing.

Cu/Ni alloys are used in thermocouples, for example, the T-type (Cu/Ni-Cu) thermocouple consists of a pure Cu leg and a Cu/Ni alloy leg. Figure 2 shows demonstration of potential applications of the process. A thin film thermopile (Figure 2A,B) and a thermocouple (Figure 2C,D) were printed using this process. The legs of these devices are pure Cu and Cu48Ni52 alloy, deposited from a single electrolyte by applying -1.6 V for pure Cu and -1.8 V for Cu48Ni52 alloy. The schematic in Figure S2 shows the process flow for Cu/Ni-Cu thermocouple printing.

In general, the performance of a thermocouple depends on the Seebeck coefficient of the metal/alloy used in each leg. The Seebeck coefficient depends on the thermal and electrical properties of the material, which are ultimately determined by the composition, among other factors. So, it can be said that if different alloys are used in the legs of the thermocouple, different performances will be obtained. The type T thermocouple is a very stable thermocouple and is used in extremely low-temperature applications such as cryogenics. The type T thermocouple consists of two legs, one made of a Copper and another leg made of Constantan (Cu 55%—Ni 45%) alloy. In our work, the Cu48Ni52 was the closest composition to the constantan alloy, so we designed the type T thermocouple using the printed pure Cu and Cu48Ni52 alloy.

Electrodeposition requires a conductive substrate as the working electrode or cathode. In our previous work, we demonstrated that a blanket sacrificial layer can be evaporated or sputtered on the substrate, and after the printing process this sacrificial layer is etched from the unwanted areas. Tungsten (W) was chosen as the sacrificial layer, since W etchant does not etch Cu or Ni. After printing of the thermocouple legs , the unwanted W coating was etched by Transene etchant TFW (Transene Company, Inc.). Approximately 300 nm alumina film was then deposited on the entire substrate as the protective layer for the thermocouple, while only the bond pads were left exposed for subsequent characterization and measurement. The entire process was

performed in a room-temperature environment. It is noted that in functional devices such as a thermocouple or thermopile, device operation depends on the junction formed between the legs made of different metals/alloys, in this case Cu and Cu/Ni alloy. Hence, the thin W sacrificial layer under both legs does not affect the device performance. A previous research study has also demonstrated continuous printing from a conductive surface to a nonconductive surface, in which the conductive surface functions as the cathode. So Such a concept is presented in electroplating of insulators.

Often, Cu/Ni–Cu thermocouples are used in cryogenic applications. A homemade apparatus including liquid nitrogen was employed for thermocouple calibration. Figure 3A shows the sensitivity response of the printed thermocouple in the temperature range of -5 °C to -65 °C. This temperature range is imposed by the limitation of the home-built calibration setup. The absolute value of the electromotive force (EMF) gradually increases as the temperature difference between the junction and bond pad decreases. The dashed line is the second-order polynomial calibration function. The slope of the EMF at a certain temperature is the Seebeck coefficient. Figure 3B shows the variation of the Seebeck coefficient with the temperature difference. The Seebeck coefficient of a thermocouple is a measure of the induced thermoelectric voltage in response to a temperature difference.

The magnetic properties of the alloy were investigated by acquiring the magnetoresistance ratio (MR) versus magnetic field, and hysteresis loops (magnetic moment vs magnetic field strength). Since copper is diamagnetic and nickel is ferromagnetic, it is expected the Cu/Ni alloy films that are rich in copper will exhibit diamagnetic behavior and vice versa. On the basis of the Lorentz force, a magnetic field applied on a material affects the movement of charged particles. The change in electric resistance versus the magnetic field refers to the magnetoresistance (MR) phenomenon. This phenomenon is useful for magnetic field sensing, for applications in magnetic recording, data storage, and manufacturing control processes. The phenomenon is quantified by the MR ratio defined as (R_0) $-R_{\rm H})/R_{\rm H}$, in which R_0 and $R_{\rm H}$ are the resistance in the absence and presence of an applied magnetic field, respectively. For ferromagnetic materials, the MR ratio is typically 5% or

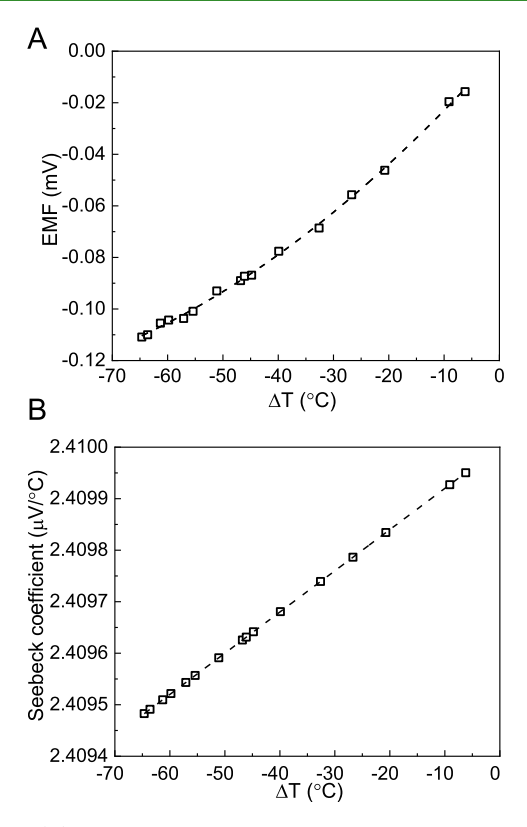


Figure 3. (A) The sensitivity response of the printed thermocouple in the cryogenic temperature region. (B) Variation of the Seebeck coefficient vs the temperature difference.

less. Magnetoresistance (MR) measurement was conducted on the printed alloy in the transverse mode, with the current perpendicular to the applied magnetic field. A magnetic field (up to 7 T) was applied perpendicular to the film plane, and the current was measured along the film plane. MR measurements showed that by increasing the Ni content the MR ratio increased, and the MR ratio was very small for the alloy with a small Ni content.

Figure 4B shows the magnetic hysteresis loops for the printed alloy, which shows M (magnetization, magnetic moment per unit volume) versus H (magnetic field strength). For this measurement, the magnetic field was applied parallel to the film plane. The hysteresis loops indicate that the Cu100-xNix film with $x \leq 52$ is nonferromagnetic, whereas clear hysteresis loops were observed for Cu31Ni69film and for higher Ni percentage. The obtained M-H responses are symmetric, and the hysteresis loss is negligible. Saturation magnetization is defined as the magnetic field in which the magnetic moments of all domains are in the same direction. The saturation magnetization of the alloy monotonically increases as the Ni content increases.

Figure S7 shows the comparison of magnetoresistance ratio, and (B) magnetic moment properties obtained in this work and the literature. Similarly, magnetic properties obtained in this work agree with the values reported in the literature for Cu/Ni alloy. The increasing trend observed in magnetic properties versus Ni concentration in our work is similar to the one experimentally and theoretically observed for bulk Cu/Ni alloys. The critical concentration of Ni in the alloy composition to show ferromagnetic behavior was reported to be ~47.6%, and the threshold for ferromagnetic behavior is correlated with the Curie temperatures. Our printed alloy

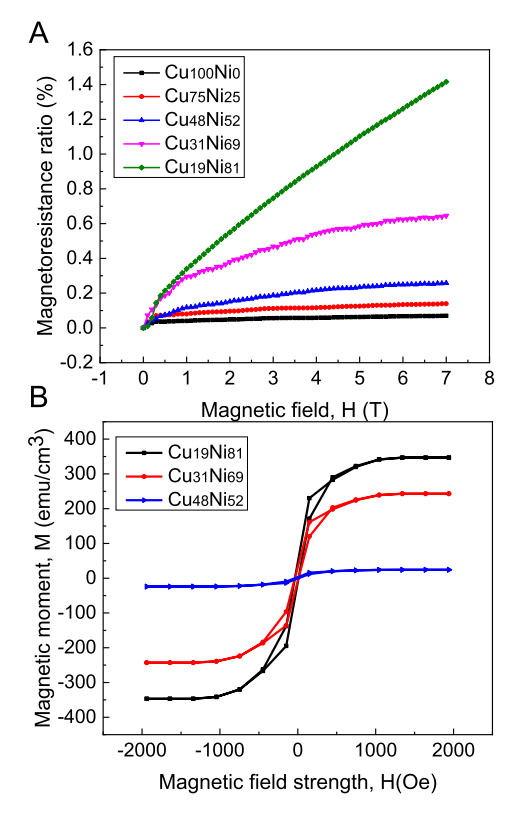


Figure 4. (A) The magnetoresistance behavior of the printed Cu/Ni alloy for different compositions. (B) The magnetic hysteresis loop of the printed Cu/Ni alloy.

also shows the ferromagnetic behavior when the Ni percentage is \sim 50%. The MR ratio of printed Cu/Ni alloy thin films are compared with our previous results of pure Ni printing, 42 and Cu/Ni alloy film prepared by bulk electroplating. 59,60 Measured saturation magnetization is very close to the reported value for Cu/Ni thin film by bulk electrodeposition. Previously reported values for magnetic saturation of Cu/Ni thin film 42,61 are included along with measured values of the current article.

Cu and Ni form a solid solution in the entire range of phase diagram since both have fcc lattices with similar lattice parameters. Figure 5A shows the X-ray diffraction (XRD) spectra of the printed Cu/Ni alloy with different compositions. Overall, the XRD analysis shows that the printed alloy is a single phase solid solution bimetallic alloy with a fcc structure.⁶² The peak for each alloy is between the fcc (111) peak of 2θ = 43.3 for pure Cu and 2θ = 44.5 for pure Ni. A shift is observed in the diffraction angle toward higher angles as the nickel content of the alloy film is increased. This is mainly attributed to the fact that the lattice parameter of Cu/Ni alloy gradually shrinks versus decreasing Cu content since the lattice parameter of Cu ($a_{Cu} = 3.6148 \text{ A}$) is larger than that of Ni (a_{Ni} = 3.5232 A). The lattice constant (a) of the Cu/Ni alloy film was determined using the Bragg's equation.⁶³ The lattice constant was found to decrease with an increase in the nickel content of the alloy film (Figure 5B) in accordance with Vegard's law. The crystallite size of the printed alloy was estimated using the Scherrer equation for the (111) peak (Table S1). Estimation gives a crystallite size in the range of 24-34 nm, confirming the nanocrystalline nature of the printed alloy.

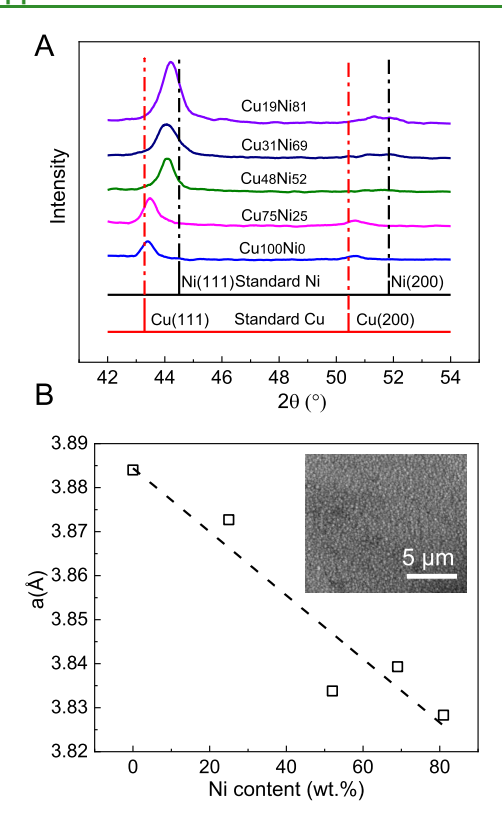


Figure 5. (A) XRD patterns of Cu/Ni alloy thin films in the $2\theta = 42-54^{\circ}$ range. The dashed lines indicate the position of the (111) fcc reflection for pure copper and pure nickel. (B) The cell parameter variation with Ni content in the alloy. The dashed line is a fit of the data using the Vegard's law. The inset shows an SEM surface image of the Cu19Ni81 alloy.

The insets in Figure 5B and Figure S3A show the SEM surface images of Cu48Ni52 alloy. Figure S3B,D shows high magnification focused ion beam (FIB) cross-section image of the alloy thin film. It can be observed that the printed alloys are continuous, uniform, and dense with no apparent porosity. Atomic force microscopy (AFM) topography image are shown in Figure S3C,E. The root-mean-square (RMS) surface roughness is ~11.5 nm, which is another indication of the nanocrystalline microstructure. He RMS surface roughness of the printed alloy versus the Ni content (wt %) is shown in Figure S4. It was found that, as the Ni content increases from zero to 81%, the surface roughness of the printed thin film

decreases from \sim 13.5 nm to \sim 11 nm, similar to the trend reported for bulk electrodeposited film.⁶⁵

The DSC spectra of the printed Cu48Ni52 alloy at heating and cooling rate of 20 °C/min acquired in N_2 atmosphere are shown in Figure 6. The DSC spectra show the melting point of the alloy at ~1192 °C (endothermic peak) with an enthalpy of 230.7 J/g. During the cooling cycle, crystallization occurs at ~1037 °C (exothermic peak) with an enthalpy of -227.4 J/g.

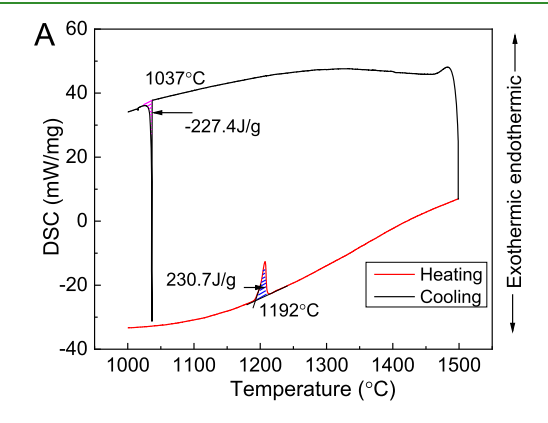
Pure metals show a single melting point in the DCS spectra; however, alloys have a melting range during which the material is a mixture of solid and liquid phases. As shown in Figure 6B, the melting temperature range for the alloy is between $T_{\rm onset}$ = 1192 °C and $T_{\rm offset}$ = 1212 °C. This range is consistent with the range reported in the literature. Overall, the information provided by DCS further confirms that the printed metal is a solid solution alloy and not a heterogeneous composite of Ni and Cu metals.

Figure 7A shows the nanoindentation elastic modulus (E) of the alloy versus the Ni content (wt %). Since the elastic modulus of Ni is higher than that for Cu, a gradual increase of E is expected with increasing Ni content. The elastic modulus of the alloy is within the values of elastic moduli of pure Cu and pure Ni. The nanoindentation hardness versus Ni content (wt %) is shown in Figure 7B. Similar to the modulus, the hardness increases with Ni content, increasing from 5.40 ± 0.16 GPa to 7.75 ± 0.3 GPa. Given the nanocrystalline microstructure of the printed films, the values of hardness are larger than those of microcrystalline Ni, Cu, and Ni/Cu alloy reported in the literature.

Figure S6 shows the comparison of the Young's modulus, and hardness obtained in this work and the literature. ⁶¹ As can be observed, the values of the Young modulus and hardness of printed Cu/Ni alloy are in rather good agreement with the values reported in ref 61, which was obtained by bulk electrodeposition. We note that the alloy in this work was obtained by 3D printing, and often 3D-printed materials show inferior properties compared to other processes, mostly due to an interlayer interface effect. However, in the case of confined electrodeposition process used in our research, metallic bonds form between each layer and hence reduce the negative impact of the interlayer.

CONCLUSION

In conclusion, a room temperature direct-write process is demonstrated for printing Cu/Ni alloy with control over



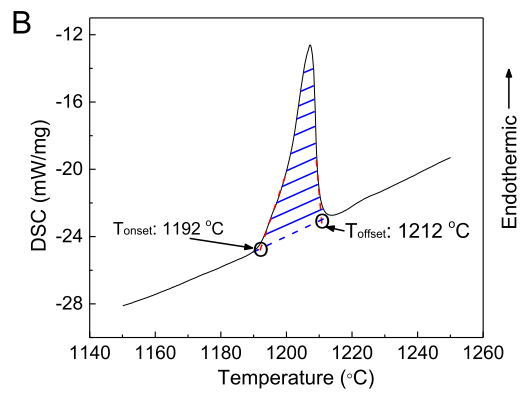


Figure 6. (A) The DSC spectra of Cu48Ni52 alloy at a heating and cooling rate of 20 $^{\circ}$ C/min in N₂ atmosphere. (B) Zoomed-in view of the DSC response in the vicinity of the melting temperature.

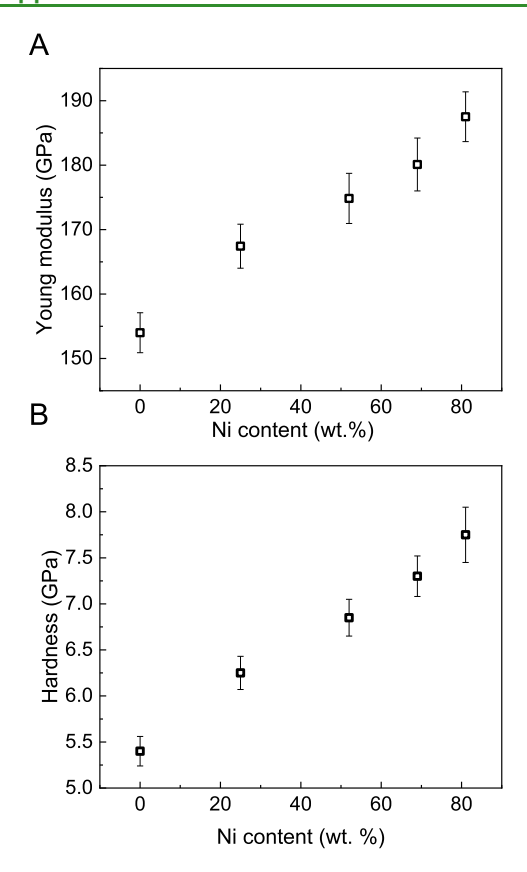


Figure 7. (A) The Young's modulus vs composition of the printed Cu/Ni alloy. (B) The dependence of hardness on the thin film composition. n = 10.

composition. The alloy is electrodeposited from a single electrolyte by changing the applied voltage to control the alloy composition. This process can enable fabrication of devices that require an interface between a metal/alloy and another alloy, such as thermocouples and heat fluxes. In addition, the process can facilitate fundamental studies on alloys by printing a continuous library of alloy composition for material characterization. The future steps can include extending the process to other alloy systems, since many alloys can be obtained using an electrodeposition process (such as Co/W, Ni/Co, Ni/W, Ni/Mo. Co/Mo, Co/W among others). The printed alloy is nanocrystalline, solid with no apparent porosity, and shows remarkable mechanical and magnetic properties. All these properties are obtained using this room-temperature process without any annealing.

MATERIALS AND METHODS

Materials. The electrolyte bath used in this study was formulated by Green. This electrolyte bath is sulfate-based and contains citrate as the complexing agent. It was found that the electrolyte with pH = 4 was unstable due to the formation of an insoluble citrate complex, while it was stable at pH = 6. The pH was adjusted by the addition of NaOH. The anode was a nickel foil (40 mm \times 10 mm \times 0.5 mm with a purity of 99.98%, Sigma-Aldrich). The anode was inserted into a plastic syringe from the backside. The printing substrate (cathode) was a silicon wafer. W etchant (TFG type from TRANSENE) consisting of less than 1% thiourea, 10–15% sodium n-nitrobenzenesulfonate, less than 10% sulfuric acid, and more than 75% water by weight was used to etch the conductive W coating after printing.

Printer Setup. Plastic pipet tips with diameters of 1.2 mm and 0.7 mm were used as the printing nozzle. The pipet tip was mounted on a

1 mL plastic syringe, which also housed the anode. Through a plastic tube, the 1 mL syringe was connected to a larger syringe (20 mL) mounted on a syringe pump (NE-300 New Era Pump). Using this setup, the electrolyte was fed to the printing area during the process. The 1 mL syringe was moved by a motorized linear stage (150 mm displacement range, Newport) along the Z-axis. The substrate was placed on an XY motorized linear stage (150 mm displacement range, Newport). Movement along the XYZ directions was controlled simultaneously using a controller based on the printing path programmed by G-code for a specific pattern. The deposition current was provided by a VersaSTAT-4 Potentiostat/Galvanostat (Princeton Applied Research).

Å <30 nm tungsten (W) film was deposited on the silicon substrate using a sputter deposition system at a base pressure better than 1×10^{-6} Torr with a deposition rate of 0.4 Å/s. The substrate was ultrasonically cleaned with acetone and isopropanol before placing in the sputter deposition chamber. To print Cu/Ni alloy, the current density was maintained at 35 mA/cm², and the nozzle speed (printing speed) was set to 0.1 mm/s. All the mentioned parameters for Cu/Ni alloy printing at this scale were achieved after a set of experiments and EDS analysis. The sputter deposited tungsten was etched using W etchant. The tungsten-coated substrate was cleaned in 5% hydroxide ammonia solution in 80 °C for 30 s prior to printing and rinsed under flowing distilled water.

FIB Cross-Section. A dual beam FEI NOVA 200 FIB was used to make cross-sections on the printed film. Each cross-section was made in several steps using a beam voltage of 30 kV and three different currents including high current (5 nA), medium current (1 nA), and low current (0.1 nA). FIB images were acquired using a low-energy ion beam (30 kV, 10 pA).

XRD. The crystal structure of the printed alloy was studied by XRD. 10 mm \times 10 mm (five layers) films were printed on a Si wafer. XRD analysis were performed in a Rigaku smartlab XRD using a Cu K_{α} radiation with a wavelength of $\lambda = 0.15406$ nm. The scanning step size and speed were Δ $(2\theta) = 0.01^{\circ}$ and 1 deg/min, respectively.

EDS Sample Preparation and Experiment. The elemental analysis was conducted using a ZEISS supra 40 scanning electron microscope (SEM). Multilayer lines (consisting of 30 layers) of Cu/Ni alloy were printed at room temperature. The EDS analysis was performed at least three times at different points for each sample.

Nanoindentation. 50-layer films were printed on a Si wafer with different compositions for the nanoindentation experiment. Roughness of the sample surface was measured by an atomic force microscope (AFM), MFP-3D-BIO (Asylum research) to estimate the approximate required indentation depth. The nanoindentation tests were performed by a NanoFlip nanoindenter (Nanomechanics, Inc.) equipped with a Berkovich tip. Indentation force in the range of 45–50 mN was applied with an indentation strain rate of 0.05 s $^{-1}$. The indentation depth was set to be less than 10% of the film thickness. Footprints of the indentations were acquired by an AFM. The elastic modulus and hardness versus the indentation depth were obtained directly from the NanoFlip nanoindentation system using the continuous stiffness measurement (CSM) technique. 70

Magnetoresistance Sample Preparation and Experiment. A physical property measurement system (PPMS, model 6000 by quantum design) was employed to measure the resistance change versus the magnetic field. The magnetic field was applied perpendicular to the current flow in the printed line. A 10-layer 10 mm linear Cu/Ni alloy line was printed on a gold (Au)-coated Si wafer for five different compositions. Four-probe connection was made to continuously measure the resistance change with respect to the magnetic field change. The resistance of the 30 nm deposited Au layer under the printed line was subtracted from the total resistance. To subtract the resistance of the initial e-beam deposited layer, we considered the printed alloy and the gold coating as two resistors connected in parallel, and the parallel resistance

$$\left(\frac{1}{R_{\text{total}}} = \frac{1}{R_{\text{LED process}}} + \frac{1}{R_{e\text{-beam process}}}\right)$$
 equation was used to obtain the

resistance of the printed alloy. No magnetoresistance was considered for gold since it does not have any magnetic property.

Magnetic Hysteresis Experiment. A 10 mm × 10 mm size (five-layer) sample was printed on a gold coated polyimide (PI) sheet for five different compositions. Magnetic hysteresis loops were acquired by a physical property measurement system (PPMS, model 6000) with a maximum applied field of 0.2 T parallel to the length direction of the printed Cu/Ni alloy. The emperature was maintained at 300 K during measurement.

Thermocouple Fabrication and Calibration. The fabricated T-type (Cu/Ni-Cu) thermocouple consists of a pure Cu leg and a Cu/Ni (Cu48Ni52) alloy leg. The printing process of the thermocouple included following steps (Figure S2). 50 nm Tungsten was deposited on a silicon wafer covered with a thermal oxide layer; a pure Cu leg Cu100Ni0 and Cu48Ni52 alloy leg were printed on top of the tungsten film, and the exposed tungsten was etched by Transene etchant (TFW Transene Company, Inc.). Alumina (300 nm) was deposited on top of the thermocouple as the protective layer. The entire printing process was conducted at room temperature.

A homemade apparatus for thermocouple calibration was used. A copper rod was submerged in a Nalgene plastic Dewar or tank filled with liquid nitrogen. A Tempco nozzle band heater was used to control the copper rod temperature above the band heater using a commercial thermocouple and a temperature controller. The printed thermocouple was placed in a slot on the upper portion of the controlled temperature area of the copper rod where an electronic thermometer with thermocouple attachment was used to measure the local temperature. Voltage was measured with a Keithley multimeter. Copper wires were fixed to the printed thermocouple using double-sided copper tape. The controller was used to change the temperature of the controlled area of the copper rod. Simultaneously, the voltage measured across the printed thermocouple was calibrated against the local temperature measured by the thermometer within the same area.

ASSOCIATED CONTENT

Supporting Information

The Supporting Information is available free of charge at https://pubs.acs.org/doi/10.1021/acsami.0c01100.

Cyclic voltammograms of the electrolyte, thermocouple fabrication process flow, SEM, AFM, and FIB images of the printed alloy, RMS surface roughness, EDS spectra, comparison of mechanical and magnetic properties with literature values (PDF)

AUTHOR INFORMATION

Corresponding Author

Majid Minary-Jolandan — Department of Mechanical Engineering, The University of Texas at Dallas, Richardson, Texas 75080, United States; oorcid.org/0000-0003-2472-302X; Email: majid.minary@utdallas.edu

Authors

Chao Wang — Department of Mechanical Engineering, The University of Texas at Dallas, Richardson, Texas 75080, United States

Md Emran Hossain Bhuiyan — Department of Mechanical Engineering, The University of Texas at Dallas, Richardson, Texas 75080, United States

Salvador Moreno – Department of Mechanical Engineering, The University of Texas at Dallas, Richardson, Texas 75080, United States

Complete contact information is available at: https://pubs.acs.org/10.1021/acsami.0c01100

Author Contributions

*C.W. and M.E.H.B. made an equal contribution.

Notes

The authors declare no competing financial interest.

ACKNOWLEDGMENTS

This work was supported by the NSF-CMMI (Award No. 1727539), the U.S. Office of Naval Research (Award No. N00014-15-1-2795), and the Department of Energy (Award No. DE-SC0017233) subcontract from UHV Technologies, Inc.

REFERENCES

- (1) Hirt, L.; Reiser, A.; Spolenak, R.; Zambelli, T. Additive Manufacturing of Metal Structures at the Micrometer Scale. *Adv. Mater.* **2017**, 29 (17), 1604211.
- (2) Ahn, B. Y.; Duoss, E. B.; Motala, M. J.; Guo, X.; Park, S.-I.; Xiong, Y.; Yoon, J.; Nuzzo, R. G.; Rogers, J. A.; Lewis, J. A. Omnidirectional Printing of Flexible, Stretchable, and Spanning Silver Microelectrodes. *Science* **2009**, 323 (5921), 1590–1593.
- (3) Skylar-Scott, M. A.; Gunasekaran, S.; Lewis, J. A. Laser-Assisted Direct Ink Writing of Planar and 3d Metal Architectures. *Proc. Natl. Acad. Sci. U. S. A.* **2016**, *113* (22), 6137–6142.
- (4) Ladd, C.; So, J. H.; Muth, J.; Dickey, M. D. 3d Printing of Free Standing Liquid Metal Microstructures. *Adv. Mater.* **2013**, 25 (36), 5081–5085.
- (5) Park, J.-U.; Hardy, M.; Kang, S. J.; Barton, K.; Adair, K.; Mukhopadhyay, D. k.; Lee, C. Y.; Strano, M. S.; Alleyne, A. G.; Georgiadis, J. G.; Ferreira, P. M.; Rogers, J. A. High-Resolution Electrohydrodynamic Jet Printing. *Nat. Mater.* **2007**, *6* (10), 782.
- (6) Lee, D.; Hwang, E.; Yu, T.; Kim, Y.; Hwang, J. Structuring of Micro Line Conductor Using Electro-Hydrodynamic Printing of a Silver Nanoparticle Suspension. *Appl. Phys. A: Mater. Sci. Process.* **2006**, 82 (4), 671–674.
- (7) Bohandy, J.; Kim, B.; Adrian, F. Metal Deposition from a Supported Metal Film Using an Excimer Laser. *J. Appl. Phys.* **1986**, *60* (4), 1538–1539.
- (8) Zenou, M.; Sa'Ar, A.; Kotler, Z. Laser Jetting of Femto-Liter Metal Droplets for High Resolution 3D Printed Structures. *Sci. Rep.* **2015**, *5*, 17265.
- (9) Wang, J.; Auyeung, R. C. Y.; Kim, H.; Charipar, N. A.; Piqué, A. Three-Dimensional Printing of Interconnects by Laser Direct-Write of Silver Nanopastes. *Adv. Mater.* **2010**, 22 (40), 4462–4466.
- (10) Botman, A.; Mulders, J.; Hagen, C. Creating Pure Nanostructures from Electron-Beam-Induced Deposition Using Purification Techniques: A Technology Perspective. *Nanotechnology* **2009**, *20* (37), 372001.
- (11) Tanaka, T.; Ishikawa, A.; Kawata, S. Two-Photon-Induced Reduction of Metal Ions for Fabricating Three-Dimensional Electrically Conductive Metallic Microstructure. *Appl. Phys. Lett.* **2006**, 88 (8), 081107.
- (12) Fan, G.; Han, Y.; Luo, S.; Li, Y.; Qu, S.; Wang, Q.; Gao, R.; Chen, M.; Han, M. Mechanism for the Photoreduction of Poly (Vinylpyrrolidone) to Haucl 4 and the Dominating Saturable Absorption of Au Colloids. *Phys. Chem. Chem. Phys.* **2016**, *18* (13), 8993–9004.
- (13) Hu, J.; Yu, M.-F. Meniscus-Confined Three-Dimensional Electrodeposition for Direct Writing of Wire Bonds. *Science* **2010**, 329 (5989), 313–316.
- (14) Daryadel, S.; Behroozfar, A.; Morsali, S. R.; Moreno, S.; Baniasadi, M.; Bykova, J.; Bernal, R. A.; Minary-Jolandan, M. Localized Pulsed Electrodeposition Process for Three-Dimensional Printing of Nanotwinned Metallic Nanostructures. *Nano Lett.* **2018**, *18* (1), 208–214.
- (15) Hirt, L.; Ihle, S.; Pan, Z.; Dorwling-Carter, L.; Reiser, A.; Wheeler, J. M.; Spolenak, R.; Vörös, J.; Zambelli, T. Template-Free 3d Microprinting of Metals Using a Force-Controlled Nanopipette for

- Layer-by-Layer Electrodeposition. *Adv. Mater.* **2016**, *28* (12), 2311–2315.
- (16) Zenou, M.; Sa'ar, A.; Kotler, Z. Laser Transfer of Metals and Metal Alloys for Digital Microfabrication of 3d Objects. *Small* **2015**, *11* (33), 4082–4089.
- (17) Gao, Y.; Li, H.; Liu, J. Direct Writing of Flexible Electronics through Room Temperature Liquid Metal Ink. *PLoS One* **2012**, *7* (9), No. e45485.
- (18) Li, H.; Yang, Y.; Liu, J. Printable Tiny Thermocouple by Liquid Metal Gallium and Its Matching Metal. *Appl. Phys. Lett.* **2012**, *101* (7), 073511.
- (19) Zheng, Y.; Zhang, Q.; Liu, J. Pervasive Liquid Metal Based Direct Writing Electronics with Roller-Ball Pen. *AIP Adv.* **2013**, 3 (11), 112117.
- (20) Longtin, J.; Sampath, S.; Tankiewicz, S.; Gambino, R. J.; Greenlaw, R. J. Sensors for Harsh Environments by Direct-Write Thermal Spray. *IEEE Sens. J.* **2004**, *4* (1), 118–121.
- (21) Schönberg, T.; Ruusuvuori, K.; Christensen, B. H.; Boivie, K.; Berild, J. P.; Ronkainen, H.; Gellein, L. T. In Surface Embedded Temperature Sensor on Tool Part for Real Time Injection Moulding Process Monitoring. 2013 Transducers & Eurosensors XXVII: The 17th International Conference on Solid-State Sensors, Actuators and Microsystems (TRANSDUCERS & EUROSENSORS XXVII) 2013, 116–119 16–20 June 2013.
- (22) Zhang, Y. L.; Mack, D. E.; Mauer, G.; Vassen, R. Laser Cladding of Embedded Sensors for Thermal Barrier Coating Applications. *Coatings* **2018**, *8* (5), 176.
- (23) Li, J.; Longtin, J. P.; Tankiewicz, S.; Gouldstone, A.; Sampath, S. Interdigital Capacitive Strain Gauges Fabricated by Direct-Write Thermal Spray and Ultrafast Laser Micromachining. *Sens. Actuators, A* **2007**, *1*33 (1), 1–8.
- (24) Liu, Y.; Ren, W.; Shi, P.; Liu, D.; Zhang, Y.; Liu, M.; Ye, Z.-G.; Jing, W.; Tian, B.; Jiang, Z. A Highly Thermostable In₂O₃/Ito Thin Film Thermocouple Prepared Via Screen Printing for High Temperature Measurements. *Sensors* **2018**, *18* (4), 958.
- (25) Offenzeller, C.; Knoll, M.; Jakoby, B.; Hilber, W. Screen-Printed, Pure Carbon-Black Thermocouple Fabrication and Seebeck Coefficients. *Sensors* **2019**, *19* (2), 403.
- (26) Zangari, G. Electrodeposition of Alloys and Compounds in the Era of Microelectronics and Energy Conversion Technology. *Coatings* **2015**, *5*, 195–218.
- (27) Lupi, C.; Pilone, D. Electrodeposition of Nickel-Cobalt Alloys: The Effect of Process Parameters on Energy Consumption. *Miner. Eng.* **2001**, *14* (11), 1403–1410.
- (28) Wu, Z. W.; Lei, Y. P.; Wang, Y.; Fu, H. G. Effect of Cobalt Content on Microstructure and Property of Electroplated Nickel-Cobalt Alloy Coatings. *Materialwiss. Werkstofftech.* **2013**, 44 (7), 593–600.
- (29) Orinakova, R.; Turonova, A.; Kladekova, D.; Galova, M.; Smith, R. M. Recent Developments in the Electrodeposition of Nickel and Some Nickel-Based Alloys. *J. Appl. Electrochem.* **2006**, *36*, 957–972.
- (30) Hasegawa, M.; Guillonneau, G.; Maeder, X.; Mohanty, G.; Wehrs, J.; Michler, J.; Philippe, L. Electrodeposition of Dilute Ni-W Alloy with Enhanced Thermal Stability: Accessing Nanotwinned to Nanocrystalline Microstructures. *Materials Today Communications* **2017**, *12*, 63–71.
- (31) Stepanova, L. I.; Purovskaya, O. G. Electrodeposition of Nickel-Based Alloys with Tungsten and Molybdenum. *Met. Finish.* **1998**, *96* (11), 50–53.
- (32) Vamsi, M. V. N.; Wasekar, N. P.; Sundararajan, G. Influence of Heat Treatment on Microstructure and Mechanical Properties of Pulse Electrodeposited Ni-W Alloy Coatings. *Surf. Coat. Technol.* **2017**, *319*, 403–414.
- (33) Detor, A. J.; Schuh, C. A. Tailoring and Patterning the Grain Size of Nanocrystalline Alloys. *Acta Mater.* **2007**, *55* (1), 371–379.
- (34) Yar-Mukhamedova, G.; Ved, M.; Sakhnenko, N.; Nenastina, T. Electrodeposition and Properties of Binary and Ternary Cobalt Alloys with Molybdenum and Tungsten. *Appl. Surf. Sci.* **2018**, 445, 298–307.

- (35) Danilov, F. I.; Vasil'eva, E. A.; Butyrina, T. E.; Protsenko, V. S. Electrodeposition of Lead-Tin Alloy from Methanesulphonate Bath Containing Organic Surfactants. *Prot. Met. Phys. Chem. Surf.* **2010**, 46 (6), 697–703.
- (36) Baskaran, I.; Sankara Narayanan, T. S. N.; Stephen, A. Pulsed Electrodeposition of Nanocrystalline Cu-Ni Alloy Films and Evaluation of Their Characteristic Properties. *Mater. Lett.* **2006**, *60* (16), 1990–1995.
- (37) Wolf, I. W. Electrodeposition of Magnetic Materials. *J. Appl. Phys.* **1962**, 33 (3), 1152–1159.
- (38) Pirota, K. R.; Navas, D.; Hernández-Vélez, M.; Nielsch, K.; Vázquez, M. Novel Magnetic Materials Prepared by Electrodeposition Techniques: Arrays of Nanowires and Multi-Layered Microwires. *J. Alloys Compd.* **2004**, 369 (1), 18–26.
- (39) Wasekar, N. P.; Sundararajan, G. Sliding Wear Behavior of Electrodeposited Ni-W Alloy and Hard Chrome Coatings. *Wear* **2015**, 342–343, 340–348.
- (40) Wasekar, N. P.; Latha, S. M.; Ramakrishna, M.; Rao, D. S.; Sundararajan, G. Pulsed Electrodeposition and Mechanical Properties of Ni-W/Sic Nano-Composite Coatings. *Mater. Des.* **2016**, *112*, 140–150.
- (41) Behroozfar, A.; Daryadel, S.; Morsali, S. R.; Moreno, S.; Baniasadi, M.; Bernal, R. A.; Minary-Jolandan, M. Microscale 3d Printing of Nanotwinned Copper. *Adv. Mater.* **2018**, *30* (4), 1705107.
- (42) Behroozfar, A.; Hossain Bhuiyan, M. E.; Daryadel, S.; Edwards, D.; Rodriguez, B. J; Minary-Jolandan, M. Additive Printing of Pure Nanocrystalline Nickel Thin Films Using Room Environment Electroplating. *Nanotechnology* **2020**, *31* (5), 055301.
- (43) Bhuiyan, M. E. H.; Behroozfar, A.; Daryadel, S.; Moreno, S.; Morsali, S.; Minary-Jolandan, M. A Hybrid Process for Printing Pure and High Conductivity Nanocrystalline Copper and Nickel on Flexible Polymeric Substrates. *Sci. Rep.* **2019**, *9* (1), 19032.
- (44) Datta, A.; Choi, H.; Li, X. Batch Fabrication and Characterization of Micro-Thin-Film Thermocouples Embedded in Metal. *J. Electrochem. Soc.* **2006**, *153* (5), H89–H93.
- (45) Lei, J.-F.; Will, H. A. Thin-Film Thermocouples and Strain-Gauge Technologies for Engine Applications. *Sens. Actuators, A* **1998**, 65 (2), 187–193.
- (46) Daryadel, S.; Behroozfar, A.; Minary-Jolandan, M. A Microscale Additive Manufacturing Approach for in Situ Nanomechanics. *Mater. Sci. Eng., A* **2019**, *767*, 138441.
- (47) Green, T.; Russell, A.; Roy, S. The Development of a Stable Citrate Electrolyte for the Electrodeposition of Copper-Nickel Alloys. *J. Electrochem. Soc.* **1998**, *145* (3), 875–881.
- (48) Pandey, R. K.; Sahu, S. N.; Chandra, S. Handbook of Semiconductor Electrodeposition; CRC Press 1996.
- (49) Podlaha, E.J.; Bonhote, C.; Landolt, D. A Mathematical Model and Experimental Study of the Electrodeposition of Ni-Cu Alloys from Complexing Electrolytes. *Electrochim. Acta* **1994**, 39 (18), 2649–2657.
- (50) Ollivier, A.; Muhr, L.; Delbos, S.; Grand, P. P.; Matlosz, M.; Chassaing, E. Copper-Nickel Codeposition as a Model for Mass-Transfer Characterization in Copper-Indium-Selenium Thin-Film Production. *J. Appl. Electrochem.* **2009**, *39*, 2337–2344.
- (51) Pellicer, E.; Varea, A.; Pane, S.; Nelson, B. J.; Menendez, E.; Estrader, M.; Surinach, S.; Baro, M. D.; Nogues, J.; Sort, J. Nanocrystalline Electroplated Cu-Ni: Metallic Thin Films with Enhanced Mechanical Properties and Tunable Magnetic Behavior. *Adv. Funct. Mater.* **2010**, 20, 983–991.
- (52) Delatorre, R. G.; Sartorelli, M. L.; Schervenski, A. Q.; Pasa, A. A.; Guths, S. Thermoelectric Properties of Electrodeposited Cuni Alloys on Si. *J. Appl. Phys.* **2003**, 93 (10), 6154–6158.
- (53) Sartorelli, M. L.; Schervenski, A. Q.; Delatorre, R. G.; Klauss, P.; Maliska, A. M.; Pasa, A. A. Cu-Ni Thin Films Electrodeposited on Si: Composition and Current Efficiency. *Physica Status Solidi* (A) **2001**, 187 (1), 91–95.
- (54) Tóth-Kádár, E.; Péter, L.; Becsei, T.; Tóth, J.; Pogány, L.; Tarnóczi, T.; Kamasa, P.; Láng, G.; Cziráki, A.; Schwarzacher, W. Preparation and Magnetoresistance Characteristics of Electrodepos-

- ited Ni-Cu Alloys and Ni-Cu/Cu Multilayers. J. Electrochem. Soc. 2000, 147 (9), 3311-3318.
- (55) Lei, Y.; Zhang, X.; Xu, D.; Yu, M.; Yi, Z.; Li, Z.; Sun, A.; Xu, G.; Cui, P.; Guo, J. Dynamic "Scanning-Mode" Meniscus Confined Electrodepositing and Micropatterning of Individually Addressable Ultraconductive Copper Line Arrays. *J. Phys. Chem. Lett.* **2018**, 9 (9), 2380–2387.
- (56) Fleury, V.; Watters, W. A.; Allam, L.; Devers, T. Rapid Electroplating of Insulators. *Nature* **2002**, *416* (6882), 716–719.
- (57) Ododo, J.; Coles, B. The Critical Concentration for the Onset of Ferromagnetism in Cuni Alloys. *J. Phys. F: Met. Phys.* **1977**, 7 (11), 2393.
- (58) Ahern, S.; Martin, M.; Sucksmith, W. The Spontaneous Magnetization of Nickel+ Copper Alloys. *Proc. R. Soc. London Ser. A. Math. Phys. Sci.* 1958, 248 (1253), 145–152.
- (59) Alper, M.; Kockar, H.; Safak, M.; Baykul, M. C. Comparison of Ni-Cu Alloy Films Electrodeposited at Low and High Ph Levels. *J. Alloys Compd.* **2008**, 453 (1–2), 15–19.
- (60) Tótĥ-Kádár, E.; Péter, L.; Becsei, T.; Tóth, J.; Pogány, L.; Tarnóczi, T.; Kamasa, P.; Láng, G.; Cziráki, Á.; Schwarzacher, W. Preparation and Magnetoresistance Characteristics of Electrodeposited Ni-Cu Alloys and Ni-Cu/Cu Multilayers. J. Electrochem. Soc. 2000, 147 (9), 3311.
- (61) Pellicer, E.; Varea, A.; Pané, S.; Nelson, B. J.; Menéndez, E.; Estrader, M.; Surinach, S.; Baró, M. D.; Nogués, J.; Sort, J. Nanocrystalline Electroplated Cu-Ni: Metallic Thin Films with Enhanced Mechanical Properties and Tunable Magnetic Behavior. *Adv. Funct. Mater.* **2010**, *20* (6), 983–991.
- (62) Zhao, B.; Shao, G.; Fan, B.; Zhao, W.; Zhang, R. Preparation and Electromagnetic Wave Absorption Properties of Novel Dendrite-Like Nicu Alloy Composite. *RSC Adv.* **2015**, *5*, 42587–42590.
- (63) Woolfson, M. M.; Woolfson, M. M. An Introduction to X-Ray Crystallography; Cambridge University Press, 1997.
- (64) Sansoz, F.; Stevenson, K.; Govinthasamy, R.; Murthy, N. Making the Surface of Nanocrystalline Ni on an Si Substrate Ultrasmooth by Direct Electrodeposition. *Scr. Mater.* **2008**, *59* (1), 103–106
- (65) Haciismailoglu, M.; Alper, M. Effect of Electrolyte Ph and Cu Concentration on Microstructure of Electrodeposited Ni-Cu Alloy Films. *Surf. Coat. Technol.* **2011**, *206* (6), 1430–1438.
- (66) Committee, A. H. Metals Handbook: Vol. 2 Properties and Selection-Nonferrous Alloys and Pure Metals; Metals Park, OH, 1978.
- (67) Chung, C. K.; Chang, W. T. Effect of Pulse Frequency on the Morphology and Nanoindentation Property of Electroplated Nickel Films. *Microsyst. Technol.* **2007**, *13* (5–6), 537–541.
- (68) Cammarata, R. C.; Schlesinger, T. E.; Kim, C.; Qadri, S. B.; Edelstein, A. S. Nanoindentation Study of the Mechanical Properties of Copper-Nickel Multilayered Thin Films. *Appl. Phys. Lett.* **1990**, *56* (19), 1862–1864.
- (69) Pellicer, E.; Pané, S.; Panagiotopoulou, V.; Fusco, S.; Sivaraman, K. M.; Suriñach, S.; Baró, M. D.; Nelson, B. J.; Sort, J. Localized Electrochemical Deposition of Porous Cu-Ni Microcolumns: Insights into the Growth Mechanisms and the Mechanical Performance. *Int. J. Electrochem. Sci.* **2012**, *7*, 4014–4029.
- (70) Hay, J.; Agee, P.; Herbert, E. Continuous Stiffness Measurement During Instrumented Indentation Testing. *Experimental Techniques* **2010**, 34 (3), 86–94.

ı

Supplementary information

Direct-Write Printing Copper-Nickel (Cu/Ni) Alloy with Controlled Composition from a Single Electrolyte using Co-electrodeposition

Chao Wang+, Md Emran Hossain Bhuiyan+, Salvador Moreno, and Majid Minary-Jolandan*

Department of Mechanical Engineering, The University of Texas at Dallas, Richardson, TX

75080, USA

*Equal contribution, *E-mail: majid.minary@utdallas.edu

Cyclic voltammograms (CV) were obtained for the pure Cu, pure Ni and Cu/Ni alloy electrolyte (Figure S1). The electrolytes were 0.04 M CuSO₄.5H₂O for Cu, 0.7 M NiSO₄.6H₂O for Ni, and 0.04 M CuSO₄.5H₂O and 0.7 M NiSO₄.6H₂O. CV responses were obtained at the tip of the same nozzle used for printing. For CV measurement, the voltage was scanned from +3V to -3V with 10 mV/s scan rate.

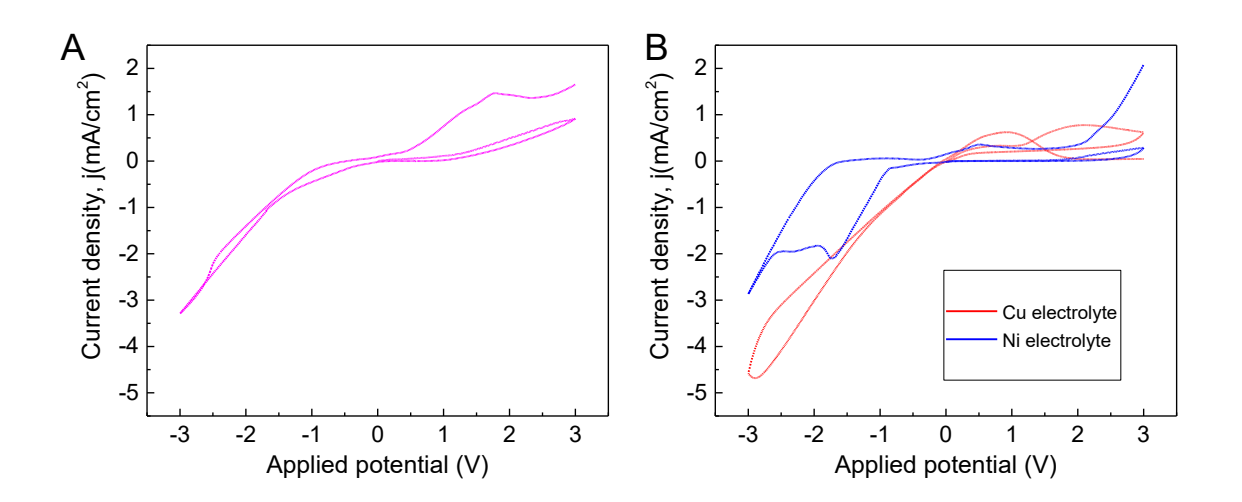


Figure S1 Cyclic voltammograms of the **(A)** Cu/Ni electrolyte containing 0.04 M CuSO₄.5H₂O and 0.7 M NiSO₄.6H₂O, and **(B)** Cu electrolyte containing 0.04 M CuSO₄.5H₂O, and Ni electrolyte containing 0.7 M NiSO₄.6H₂O.

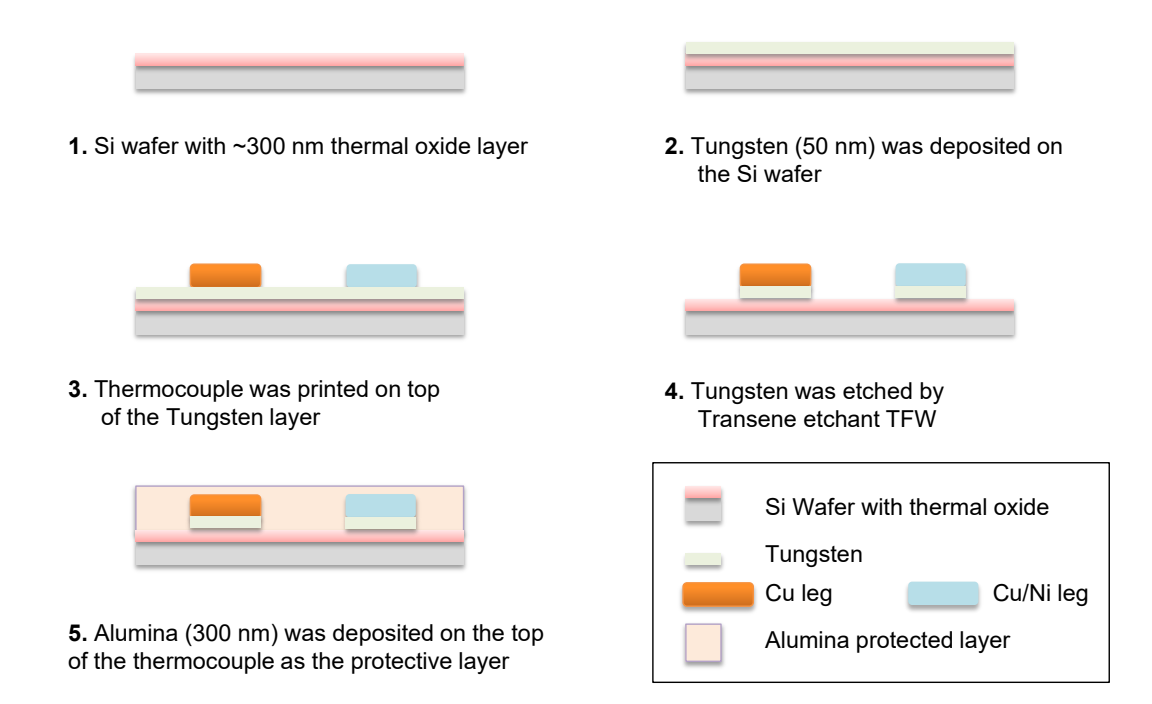


Figure S2 The schematic shows the process flow for Cu – Cu/Ni thermocouple printing.

Table S1 Structural data obtained from XRD analysis (lattice parameter *a*, and crystallite size <*D*>).

Alloy composition	Lattice cell parameter (a)	Crystallite size < D> nm
Cu100Ni0	3.884	29
Cu75Ni25	3.873	34
Cu48Ni52	3.839	28
Cu31Ni69	3.834	24
Cu19Ni81	3.828	28

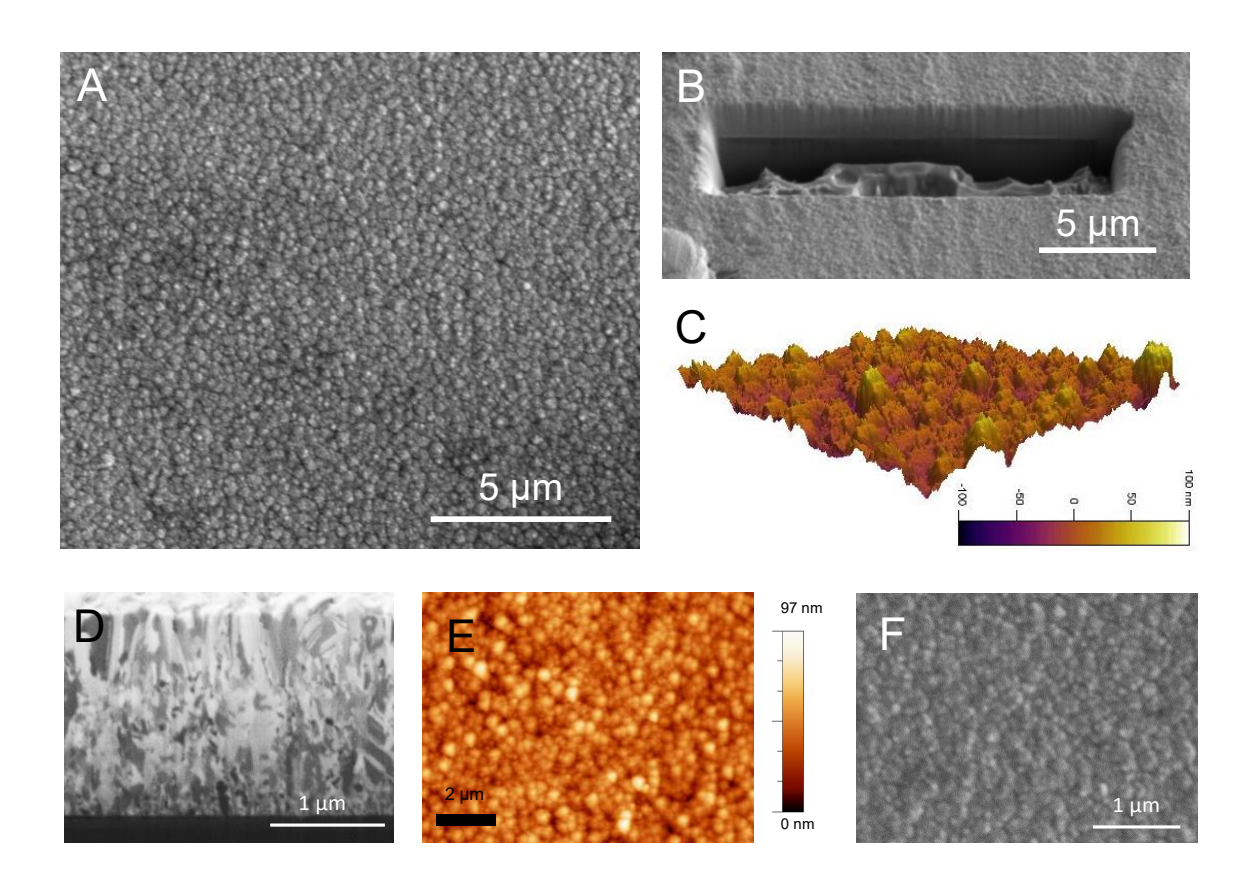


Figure S3 (A) and (F) The SEM surface morphology, **(B) and (D)** the FIB-milled cross-section, and **(C) and (E)** the AFM topography image for Cu/Ni alloy printed under 1.8 V deposition voltage.

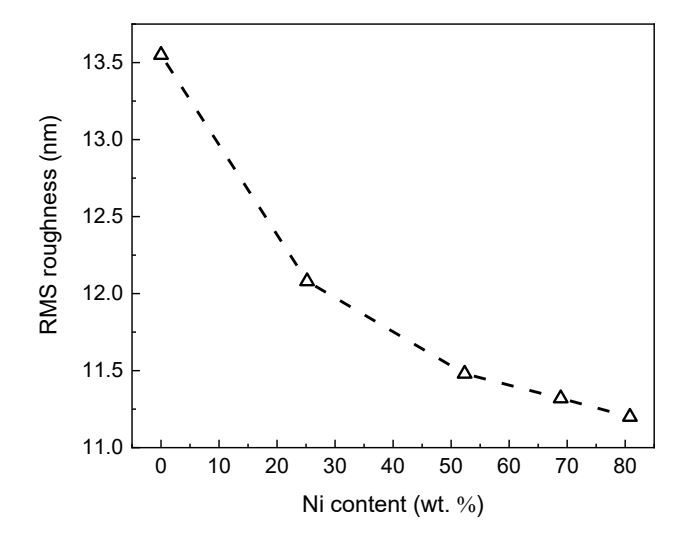


Figure S4 The RMS surface roughness of the printed alloy vs. the Ni content (wt. %).

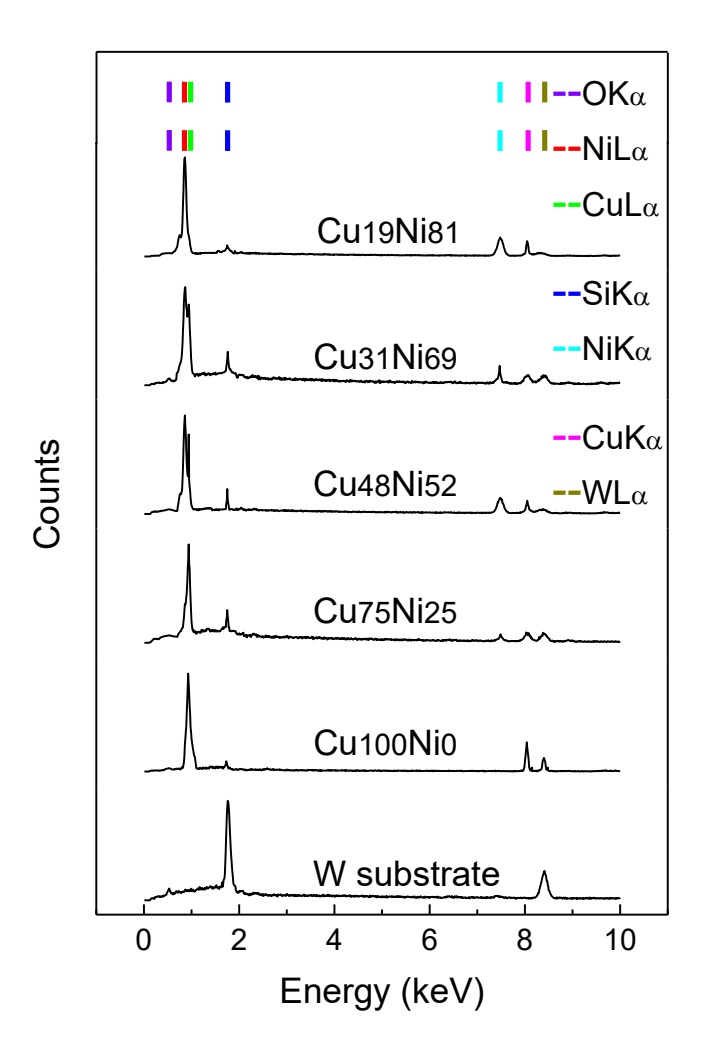


Figure S5 The EDS spectra for Cu/Ni alloys deposited under various voltage. The EDS spectrum of the W substrate is also included. The peaks are color-coded based on the colors shown in the caption.

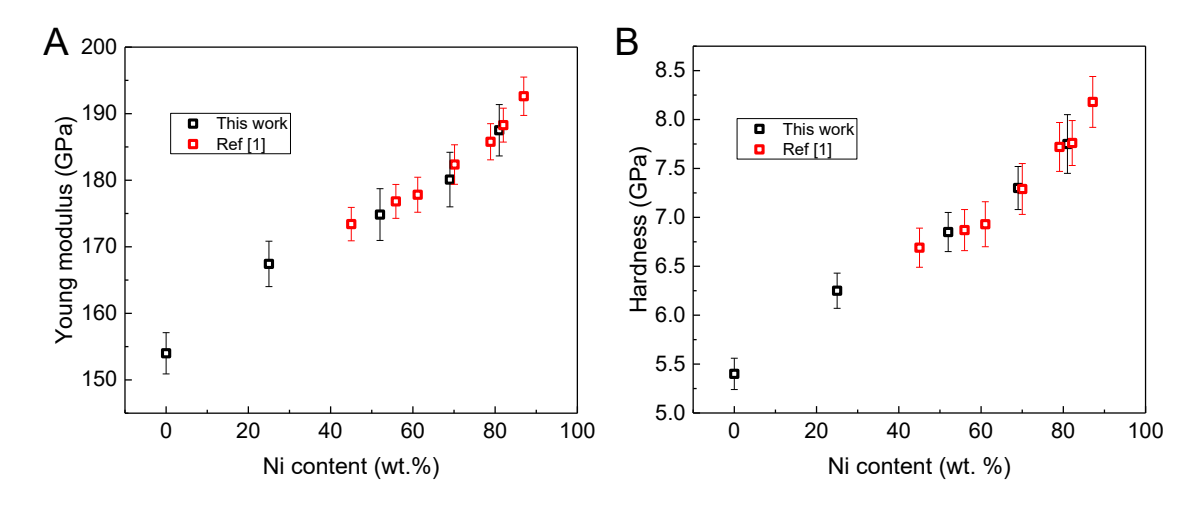


Figure S6 The comparison of **(A)** the Young's modulus, and **(B)** hardness obtained in this work and the literature.

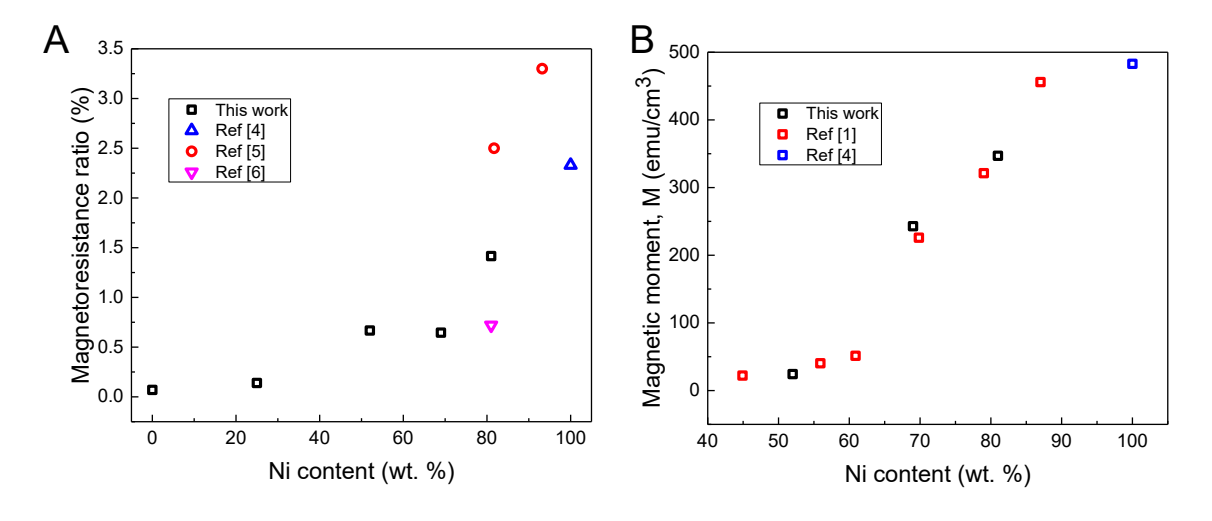


Figure S7 The comparison of **(A)** magnetoresistance ratio, and **(B)** magnetic moment properties obtained in this work and the literature.

Refences

- 1. Pellicer, E.; Varea, A.; Pané, S.; Nelson, B. J.; Menéndez, E.; Estrader, M.; Surinach, S.; Baró, M. D.; Nogués, J.; Sort, J., Nanocrystalline Electroplated Cu–Ni: Metallic Thin Films with Enhanced Mechanical Properties and Tunable Magnetic Behavior. *Advanced Functional Materials* **2010**, *20* (6), 983-991.
- 2. Ododo, J.; Coles, B., The Critical Concentration for the Onset of Ferromagnetism in Cuni Alloys. *Journal of Physics F: Metal Physics* **1977**, *7* (11), 2393.
- 3. Ahern, S.; Martin, M.; Sucksmith, W., The Spontaneous Magnetization of Nickel+ Copper Alloys. *Proceedings of the Royal Society of London. Series A. Mathematical and Physical Sciences* **1958**, *248* (1253), 145-152.
- 4. Behroozfar, A.; Bhuiyan, M. E. H.; Daryadel, S.; Edwards, D.; Rodriguez, B. J.; Minary-Jolandan, M., Additive Printing of Pure Nanocrystalline Nickel Thin Films Using Room Environment Electroplating. *Nanotechnology* **2019**, *31* (5), 055301.
- 5. Alper, M.; Kockar, H.; Safak, M.; Baykul, M. C., Comparison of Ni–Cu Alloy Films Electrodeposited at Low and High Ph Levels. *Journal of Alloys and Compounds* **2008**, *453* (1-2), 15-19.
- 6. Tóth-Kádár, E.; Péter, L.; Becsei, T.; Tóth, J.; Pogány, L.; Tarnóczi, T.; Kamasa, P.; Láng, G.; Cziráki, Á.; Schwarzacher, W., Preparation and Magnetoresistance Characteristics of Electrodeposited Ni-Cu Alloys and Ni-Cu/Cu Multilayers. *Journal of The Electrochemical Society* **2000**, *147* (9), 3311.